

Linking mixing and flow topology in porous media: An experimental proofMónica Basilio Hazas ¹, Francesca Ziliotto ¹, Massimo Rolle ², and Gabriele Chiogna ^{1,*}¹*Chair of Hydrology and River Basin Management, Technical University of Munich, Arcisstraße 21, 80333 Munich, Germany*²*Department of Environmental Engineering, Technical University of Denmark, 2800 Kongens Lyngby, Denmark*

(Received 22 June 2021; accepted 25 February 2022; published 16 March 2022)

Transport processes in porous media are controlled by the characteristics of the flow field which are determined by the porous material properties and the boundary conditions of the system. This work provides experimental evidence of the relation between mixing and flow field topology in porous media at the continuum scale. The setup consists of a homogeneously packed quasi-two-dimensional flow-through chamber in which transient flow conditions, dynamically controlled by two external reservoirs, impact the transport of a dissolved tracer. The experiments were performed at two different flow velocities, corresponding to Péclet numbers of 191 and 565, respectively. The model-based interpretation of the experimental results shows that high values of the effective Okubo-Weiss parameter, driven by the changes of the boundary conditions, lead to high rates of increase of the Shannon entropy of the tracer distribution and, thus, to enhanced mixing. The comparison between a hydrodynamic dispersion model and an equivalent pore diffusion model demonstrates that despite the spatial and temporal variability in the hydrodynamic dispersion coefficients, the Shannon entropy remains almost unchanged because it is controlled by the Okubo-Weiss parameter. Overall, our work demonstrates that under highly transient boundary conditions, mixing dynamics in homogeneous porous media can also display complex patterns and is controlled by the flow topology.

DOI: [10.1103/PhysRevE.105.035105](https://doi.org/10.1103/PhysRevE.105.035105)**I. INTRODUCTION**

Theoretical studies have shown that flow topology, understood as the characteristics of the fluid described in terms of a vector field [1], may have a strong influence on dilution and mixing processes [2–7]. For instance, radial flows [8–10], convective transfer [11,12], and vortex structures [3,13] can control reaction dynamics. At low Reynolds numbers, mixing is often slow but it can be enhanced by transient flow conditions with important applications in fields such as biology, medicine, and engineering [14–21]. Particularly complex is the case of mixing processes in porous media and microchannels, where flow dynamics and mixing are further complicated by the complex structure of the pore space [22–29]. At the continuum scale, heterogeneities and anisotropies in the porous material [30–32], or external forcing, such as applied voltages [33], moving objects such as artificial cilia [34] or prisms [35] within microchannels, source-sink pulses [36–41], and periodic boundaries [42–46], can lead to heterogeneous flow fields, which in turn can generate a wide range of stretching and folding behaviors [30,47,48], affect dispersion [49,50], and enhance mixing [51–53].

Mixing processes are often enhanced when the interface of a solute with the surroundings enlarges, thus increasing diffusive and dispersive fluxes [37]. Therefore, the quantification of mixing in porous media can be approached by analyzing the evolution of the concentration distribution of a solute plume,

using, for example, the dilution index [54]. The dilution index measures the state of dilution of a system, where a larger number indicates that a solute is more uniformly distributed and occupies a larger volume of the fluid. This index can be expressed in its logarithmic form as the Shannon entropy of the spatial distribution of the solute concentration. Other approaches to quantify mixing are based on the relation between flow topology and plume deformation. In this sense, a topological analysis can be done through the Okubo-Weiss function [55,56], commonly used in fluid mechanics to distinguish filament from vortex structures in two-dimensional flow fields and with applications in the study of turbulence [57,58] and vortex stability [59], as well as in geophysical fluids [60–62], cellular flows [63], and germ spread [64]. Positive Okubo-Weiss values correspond to filament structures, which are found in regions where shear and stretching forces dominate over vorticity, causing hyperbolic motion in the fluid [56], and are associated with mixing hot spots [65]. Negative Okubo-Weiss values indicate values of dominating vorticity. De Barros *et al.* [65] identified a relation between the evolution of the Shannon entropy and the effective Okubo-Weiss parameter (defined as the average positive Okubo-Weiss value over the plume area) in a heterogeneous steady-state flow. Wright *et al.* [66] found that reaction hot spots in a two-dimensional (2D) idealized heterogeneous porous medium were associated with the regions where the Okubo-Weiss parameter was highest, and Engdahl *et al.* [67] obtained a positive correlation between the Okubo-Weiss field and the maximum increase of the collocation density, understood as the likelihood that reactive particles will occupy the same space.

*gabriele.chiogna@tum.de

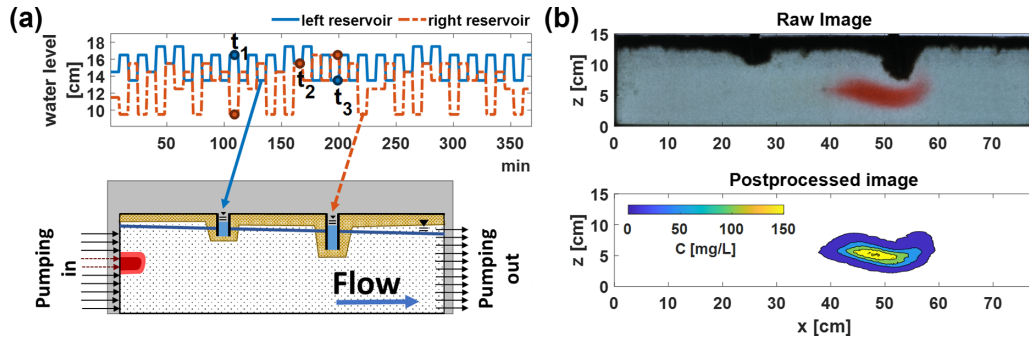


FIG. 1. (a) Sketch of the flow-through experimental setup with fluctuations in the water level of the reservoirs applied in the experiment Pe200, where times t_1 (109 min), t_2 (166 min), and t_3 (199 min) correspond to the times shown in the flow and transport analysis of Figs. 2 and 3. (b) Tracer plume observed, as raw and postprocessed images, at $t = 170$ min for the experiment Pe200.

Both numerical (e.g., [26,47,54,65–67]) and experimental studies (e.g., [24,48,68,69]) investigating flow topology and mixing in porous media generally consider steady-state flow conditions. Most research including time-dependent flows has been theoretical (for example, uniform fluctuating boundaries [42,44,49], or dipole and quadrupole configurations [37,70]), with only a few exceptions based on experimental data [71,72]. For instance, some works have focused on how fluctuating flow fields generate chaotic advection [37,38,41,42,70] and affect dispersion coefficients [44,46,49,50,73–75] with an overall increase in dispersion, spreading, and mixing. In this contribution, we use experimental data from a quasi-2D flow-through chamber subject to two time-dependent boundary conditions to analyze the dilution of a solute tracer. The chamber is packed with a homogeneous porous medium in order to isolate the effect of the transient flow field. We performed experiments at two different flow velocities and considering different fluctuations of the dynamic boundaries. Image analysis was employed to quantify the evolution of spreading and mixing of the dye color tracer in the transient flow field. The model-based interpretation of the experimental results allows us to identify the relation between the dynamics of solute mixing under transient flows, quantified through the temporal change of the plume entropy, and the topology of the flow.

II. MATERIAL AND METHODS

A. Flow-through experiments

Figure 1(a) shows a sketch of the experimental setup. The quasi-two-dimensional flow-through chamber has inner dimensions of $77.9 \times 15 \times 1.1 \text{ cm}^3$. Ten inlet and 11 outlet ports on the left and right side of the system, respectively, are equally spaced by 1.1 cm and are connected to two high-precision multichannel peristaltic pumps (IPC-N24, Cole-Parmer). Each port injects (extracts) $7.6 \times 10^{-9} \pm 4.17 \times 10^{-10} \text{ m}^3/\text{s}$, creating fixed flux boundary conditions on the left (right) sides. The system is water saturated and filled with a homogeneous porous medium consisting of glass beads with particle diameter $d_p = 1\text{--}1.5 \text{ mm}$ (mean 1.25 mm), with an average hydraulic conductivity of $1.27 \times 10^{-2} \text{ m/s}$ and a porosity of 0.4. The choice of the particle size was done in order to have permeable material that allowed a good hydraulic connection between the porous medium and the

dynamic boundaries. A wet packing procedure, consisting in progressively rising and maintaining the water level above the porous medium, was applied to avoid air entrapment [76]. The chamber is filled on the top with a finer sand layer [yellow color in the Fig. 1(a)] to avoid the occurrence of preferential flow. Two water reservoirs are connected to the flow-through chamber, at a distance of approximately one-third and two-thirds of the chamber length, and act as head-dependent flux boundaries. Each water reservoir was placed on an electric lift. By adjusting the height of the lift, changes in the water level were imposed at a time interval $\tau = 8 \text{ min}$, thus generating transient flow fields [see water level in Fig. 1(a)]. Despite the continuous exchange of water between the water reservoirs and the flow-through chamber, variations in the water level in the reservoir are negligible due to their large size. To study dilution and mixing processes, we injected a conservative tracer (New Coccine, CAS 2611-82-7, Sigma-Aldrich) from $t_{i1} = 8 \text{ min}$ to $t_{i2} = 32 \text{ min}$ and tracked the tracer plume across the chamber using a digital camera, Nikon D5000 [Fig. 1(b)]. From the recorded pictures, we estimated the concentration of the plume at high spatial and temporal resolution (60 pictures per hour and 135 ppi) following a procedure similar to the one proposed by Jaeger *et al.* [77]. A full description of the flow-through chamber configuration and the optical calibration of the images can be found in [71].

While in [71] we analyzed steady-state and transient flow experiments to study mixing enhancement by transient boundary conditions considering different phase shifts and amplitudes, here we focus on the comparison of two experiments with two different Péclet numbers. Therefore, in this study, we present two experiments in which the pumping rates established a predominantly horizontal flow with different grain Péclet numbers, defined as $Pe = |v|d_p/D_{aq}$ [—], where v [LT^{-1}] is the average pore water or seepage velocity, and D_{aq} [L^2T^{-1}] is the aqueous diffusion coefficient that for the tracer New Coccine at 20°C is equal to $3.6 \times 10^{-10} \text{ m}^2/\text{s}$ [77]. The Péclet number in the two flow-through experiments is $Pe = 191.0 \pm 63.4$ and $Pe = 565.1 \pm 63.5$, respectively. For the sake of simplicity, we refer to these two flow-through experiments as Pe200 and Pe570.

B. Flow and transport modeling

To obtain a quantitative interpretation of the experiments, we run flow and transport simulations and validate them with

the tracer observations. The model also allows us to obtain a fully resolved velocity field, considering as boundary conditions the measured inlet and outlet pumping rates at each port of the flow-through chamber, as well as the fluctuating hydraulic heads in the reservoirs.

The transient flow equation is derived combining Darcy's law with the continuity equation over a representative elementary volume, yielding

$$S \frac{\partial h}{\partial t} = \nabla \cdot (-\mathbf{K} \cdot \nabla h) + \mathbf{q}', \quad (1)$$

where \mathbf{K} [LT^{-1}] is the hydraulic conductivity tensor, $\nabla h[-]$ the hydraulic head gradient, $\mathbf{q}'[LT^{-1}]$ accounts for sources and sinks, and $S[-]$ is the storage coefficient. The flow simulations are solved with the finite difference model MODFLOW MF-OWHM [78], considering a discretization of the two-dimensional domain of 1140 columns ($\Delta x = 0.068$ cm) and 395 layers ($\Delta z_{min} = 0.027$ cm). The time-dependent boundary conditions are treated as a head-dependent flux. The finite differences equations are solved with a Newton-Raphson formulation capable of handling model cells that are drying and rewetting as a consequence of the oscillations in the water level [78].

The transport equation for a conservative tracer is described by the advection-dispersion equation:

$$\frac{\partial(nC)}{\partial t} = \nabla \cdot (n\mathbf{D}\nabla C) - \nabla \cdot (n\mathbf{v}), \quad (2)$$

where $C[ML^{-3}]$ is the tracer concentration, $n[-]$ is the porosity, \mathbf{v} is the seepage velocity, and $\mathbf{D}[L^2T^{-1}]$ is the dispersion tensor. The transport simulations are calculated with a modified version of MT3D-USGS [79] that implements a linear, grain size (d_p) specific parametrization for the longitudinal dispersion coefficient [80,81],

$$D_L = D_P + \frac{1}{2}d_p v, \quad (3)$$

and a nonlinear, grain size, and compound specific parametrization for the transverse dispersion coefficient [82,83],

$$D_T = D_P + D_{aq} \left(\frac{Pe^2}{Pe + 2 + 4\delta^2} \right)^\beta, \quad (4)$$

where $D_P = D_{aq}n[L^2T^{-1}]$ denotes the pore diffusion coefficient, $\delta[-]$ is the ratio between the length of a pore channel and its hydraulic radius, and $\beta[-]$ is an empirical exponent to capture the degree of incomplete mixing in pore channels. We use values of $\beta = 0.5$ and $\delta = 5.37$ based on the compilation of transverse dispersion experiments presented in [83].

We refer to the dispersion model described by Eqs. (3) and (4) as the hydrodynamic dispersion model ($D_T D_L$).

Additional simulations were performed considering only the velocity-independent pore diffusion term from Eqs. (3) and (4), but designed to reach the same dilution as the hydrodynamic dispersion model under the same velocity field. This was done by using a larger equivalent pore diffusion coefficient. To distinguish this model from the previous one, we identify it as the equivalent pore diffusion model ($D_{P,eq}$).

III. FLOW TOPOLOGY AND MIXING METRICS

A. Okubo-Weiss parameter

The topology of a two-dimensional flow field can be described in terms of stretching $\alpha [T^{-1}]$, shear $\sigma [T^{-1}]$, and vorticity $\omega [T^{-1}]$. Following [55,65], these quantities are defined by partial derivatives of the velocity field as follows:

$$\alpha = 2 \frac{\partial v_x}{\partial x}, \quad \sigma = \frac{\partial v_z}{\partial x} + \frac{\partial v_x}{\partial z}, \quad \omega = \frac{\partial v_z}{\partial x} - \frac{\partial v_x}{\partial z}, \quad (5)$$

where x and z are the components in the horizontal and vertical directions, respectively. The Okubo-Weiss parameter $\Theta [T^{-2}]$ is then calculated as [55,56]

$$\Theta = (\alpha^2 + \sigma^2) - \omega^2. \quad (6)$$

Therefore, positive values indicate areas where shear and stress dominate, while negative values characterize vorticity dominating zones. While this parameter can be used to study local mixing strength in porous media [61,65,66], we focus on global mixing properties and therefore also calculate the effective Okubo-Weiss function $\Theta^e(t)$ following [65]

$$\Theta^e(t) = \frac{\sum \Theta(\mathbf{x}, t) H[\Theta(\mathbf{x}, t)] F_5[C(\mathbf{x}, t)] \Delta X \Delta Z}{\sum H[\Theta(\mathbf{x}, t)] F_5[C(\mathbf{x}, t)] \Delta X \Delta Z}, \quad (7)$$

where $\Theta(\mathbf{x}, t)$ and $C(\mathbf{x}, t)$ are the Okubo-Weiss function and tracer concentration estimated at time t over the space coordinates \mathbf{x} [L], $H(y)$ is the Heaviside step function, and $F_5(y)$ is a step function for concentrations higher than 5 mg/l, which is the limit of detection of the imaging method for the solute concentrations in the flow-through experiments. The computation of the Okubo-Weiss function and, thus, of the effective Okubo-Weiss parameter requires the computed fully resolved flow field.

B. Dilution index

The pictures from the experiment and the conservative transport model provide qualitative and quantitative data of the tracer plume distribution, its concentration, and its temporal evolution in the domain. Using this information, it is possible to quantify the dilution of the tracer plume in both the experiments and the simulations based on the dilution index, $E(t)$, which is defined as [54]

$$E(t) = \exp \left[- \int_V p(\mathbf{x}, t) \ln p(\mathbf{x}, t) dV \right], \quad (8)$$

where $p(\mathbf{x}, t) [L^{-3}]$ is defined as the concentration of the solute tracer normalized by its total mass and is a probability density function:

$$p(\mathbf{x}, t) = \frac{C(\mathbf{x}, t)}{\int_V C(\mathbf{x}, t) dV}, \quad (9)$$

being V is the total volume of the domain. The dilution index is commonly interpreted as the exponential of the Shannon entropy of the plume, $\ln E(t)$ [54].

In addition, we compute the rate of increase of the entropy $d \ln E(t) / dt$, which is a measure of the kinetics of dilution and represents how quickly the plume occupies a progressively larger volume as it is transported in the porous medium.

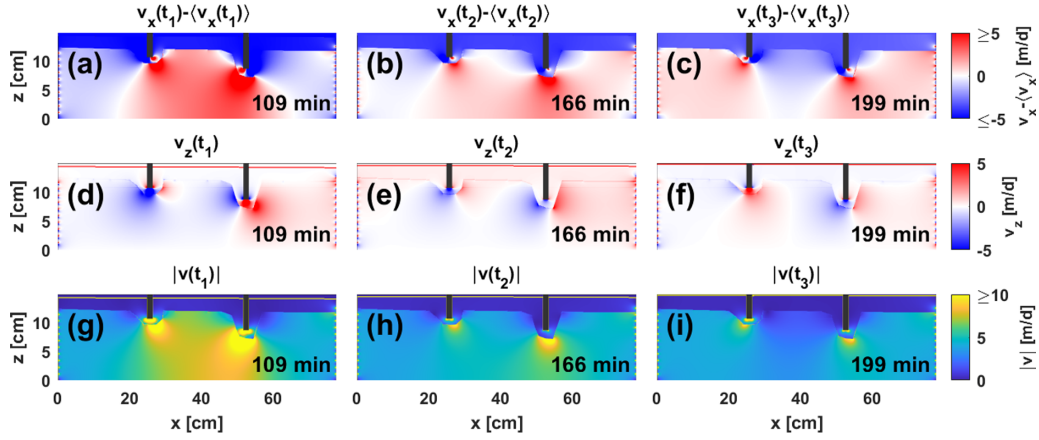


FIG. 2. (a)–(c) Horizontal seepage velocity field expressed as difference between the seepage velocity (in meters per day) and its spatial mean at the specific time steps indicated, (d)–(f) vertical seepage velocity field, and (g)–(i) magnitude of the velocity field for three selected times for the experiment Pe200 [the selected times are marked in Fig. 1(a)].

IV. RESULTS AND DISCUSSION

A. Flow field analysis

To analyze the impact of the fluctuating boundaries on the flow field, Fig. 2 shows maps of the simulated velocities at selected times $t_1 = 109$, $t_2 = 166$, and $t_3 = 199$ min. These three time steps correspond to three different water level conditions in the reservoirs [Fig. 1(a)] leading to three different velocity fields. At t_1 , the hydraulic head of the left reservoir is 6 cm higher than the right reservoir. This accelerates the fluid motion in the horizontal direction, in particular in the area between both reservoirs [Figs. 2(a) and 2(g)]. It also shows that for this time step, the water flows from the left reservoir towards the saturated porous medium, while the opposite occurs for the right reservoir [Fig. 2(d)]. At t_2 , the water level in both reservoirs is similar and although in both cases the water flows in the porous medium, the changes in the velocity field are smaller than at t_1 . At t_3 , the hydraulic head of the right reservoir is higher than that of the left reservoir. The velocity in the mean direction of the flow decreases in the area between both reservoirs [Figs. 2(c) and 2(i)]. In the vertical direction, we observe a flow reversal of the water compared to t_1 . In this case, water flows from the saturated porous medium to the left reservoir, and from the right reservoir into the saturated porous medium [Fig. 2(f)]. Overall, we observe that the variations in the velocity field in our system directly result from the oscillating boundaries.

Figures 3(a)–3(c) and 3(d)–3(f) show, respectively, the images of the tracer plume and the maps of the Okubo-Weiss parameter $\Theta(x)$ for the selected times. For all velocity fields, the Okubo-Weiss value is mainly positive (over 97% of the active cells), indicating that strain and stretching are dominating in the system over vorticity. A reason may be the homogeneity of the porous medium. In fact, Geng *et al.* [61], who simulated transient groundwater flows subject to tidal boundaries, also observed that vorticity regions were only present in simulations with heterogeneous hydraulic conductivity fields. In our setup, the regions closer to the reservoirs and the zones with a change in the longitudinal velocity field display higher $\Theta(x)$ values. On the contrary, between the reservoirs the $\Theta(x)$ seems to be lower [Fig. 3(d)] even if

the v_x is higher [Fig. 2(a)], meaning that the change in the velocity field is the main controlling factor for the observed stretching. In addition, to visualize how the topology of the flow field affects the plume in our setting, Figs. 3(g)–3(i) show the effective Okubo-Weiss values. Here we can notice that the part of the plume passing below the fluctuating reservoir displays the highest effective Okubo-Weiss values.

B. Solute transport analysis

Since the duration of the injection between the two experiments was kept constant, the experiment performed at Pe570 had more injected mass than the experiment at Pe200 and thus it reached larger values of the dilution index. To make the result comparable, we normalized the value of the Shannon entropy by the simulated entropy of the plume at t_p , which represents the time when the tracer plume was completely injected in the system. We will refer to this entropy value as initial entropy. Figure 4 shows the modeled and measured Shannon entropy of the tracer plume normalized by its initial entropy in both flow-through experiments. In this and in the following figures, we show the time as the dimensionless quantity t/τ . Despite the slight overestimation of the normalized entropies during some time intervals, we observe that there is good agreement between the simulations and the experiment (root mean square error is 0.025 and 0.004 for Pe200 and Pe 570, respectively). This comparison helps us to validate our model results. The normalized entropy in both cases is increasing monotonically. Despite the larger volume of the plume at Pe570, the normalized entropy at Pe200 reaches higher values. This is partly because both plumes dilute at a very similar speed—in fact, the lines of the normalized entropy are almost superposed—and, as the plume at Pe200 spends more time in the domain, it has more time for dilution.

We investigate first the relation between the effective Okubo-Weiss parameter and the rate of increase of the entropy by wavelet coherence (Fig. 5). The wavelet coherence can be interpreted as the local correlation coefficient between the time series in the time-frequency domain [84]. In the coherence plot, the color code represents the value of the coherence

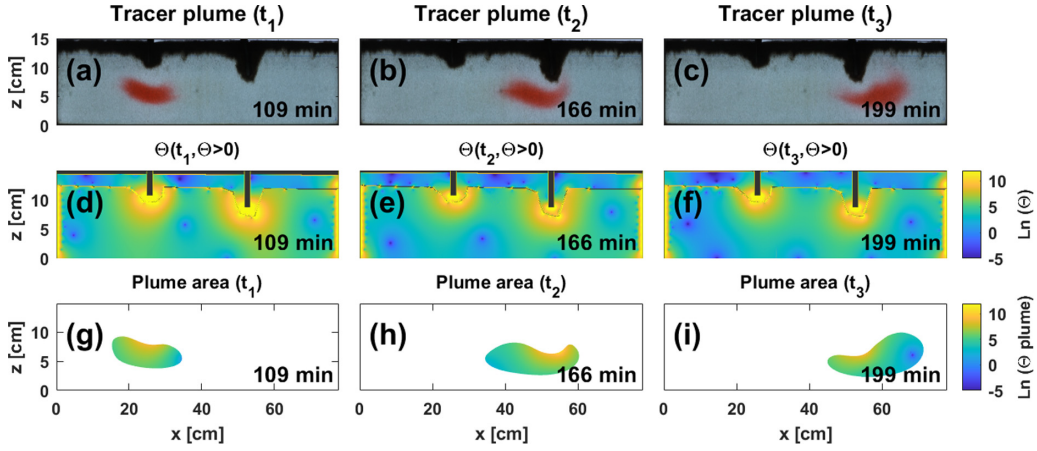


FIG. 3. (a)–(c) Images of the tracer plume, (d)–(f) natural logarithm of the positive Okubo-Weiss field, and (g)–(i) local value of the Okubo-Weiss parameter in the area of the solute plume for the three different times for the experiment Pe200 shown in Fig. 1(a).

that can change in time (x axis) and depending on the period (y axis). Here, $\ln \Theta^e(t)$ and $d \ln E(t)/dt$ are coherent, in particular, starting from $t/\tau = 13$, which corresponds to the time at which the centroid of the plume passes below the first reservoir. Special attention is focused at the period of 16 min, where the right-pointing arrows between 13 and 20 in the wavelet coherence indicate that $\ln \Theta^e(t)$ and $d \ln E(t)/dt$ are in phase. After 20, the two time series start losing phase, although they remain coherent.

In general, the relation between both metrics can also be seen in the time series of both the effective Okubo-Weiss parameter [Fig. 6(a), right axis] and the entropy rate of increase [Fig. 6(a), left axis], where both metrics display square waves with a period of 16 min resulting directly from the fluctuations in the transient boundary conditions. In fact, by comparing fluctuations of the reservoirs [Fig. 1(a)] with the Okubo-Weiss parameter, it is possible to observe that the crest of the wave of $\ln \Theta^e(t)$ corresponds to the times at which the water level of the left reservoir is higher than the right one. This can be

explained because the stress imposed on the system is higher, in particular as the reservoir fluctuations are in counterphase.

In the experiment at Pe570, the dilution rate and the effective Okubo-Weiss parameter also show a square wave behavior and are almost in phase [Fig. 6(b)]. However, due to the shorter duration of the experiment, we cannot perform a wavelet coherence analysis since the period of 16 min is outside the cone of influence.

The oscillations observed in $d \ln E/dt$ are more affected by the dynamics of the flow field in the area between both water reservoirs. Mixing enhancement, therefore, occurs mainly in the area between the reservoirs, as seen in Figs. 3(d)–3(f). At Pe200, the fluctuations in $d \ln E/dt$ are stronger once the centroid of the plume travels below the first reservoir at $t/\tau = 12.75$. Then, they become weaker after the plume passes the second reservoir at approximately $t/\tau = 25$, even if the effective Okubo-Weiss parameter is high and its oscillations are strong. This result can be explained by the fact that, at the beginning and at the end of the flow-through system, the flow field is dominated by the fixed flux boundary conditions established through the pumps, and therefore the influence of the transient reservoir boundaries on plume deformation is less pronounced.

Besides the changes in the flow topology, a variable flow field also impacts the local dispersion coefficient, which ultimately affects mixing. In the physical experiment we cannot eliminate the effect of variable velocity on hydrodynamic dispersion. To confirm that mixing enhancement is controlled by the effective Okubo-Weiss parameter, we performed numerical simulations using the equivalent pore diffusion model (see Fig. 4, black lines). The effective pore diffusion coefficients were 20 and 30 times larger than D_p for Pe200 and Pe570, respectively. In Figs. 6(a) and 6(b) we observe that even if we exclude the effect of the variable flow field on the hydrodynamic dispersion tensor, both $d \ln E/dt$ and Θ^e remain basically unchanged. Figures 7(a)–7(f) and 7(h)–7(m) show the spatial variability of the local hydrodynamic dispersion normalized by the aqueous diffusion coefficient at different selected times, as well as the mean value of the normalized local dispersion for both $D_T D_L$ and $D_{P,eq}$ at the Pe200 and Pe570. Overall, we observe in Figs. 7(g) and 7(n) that the

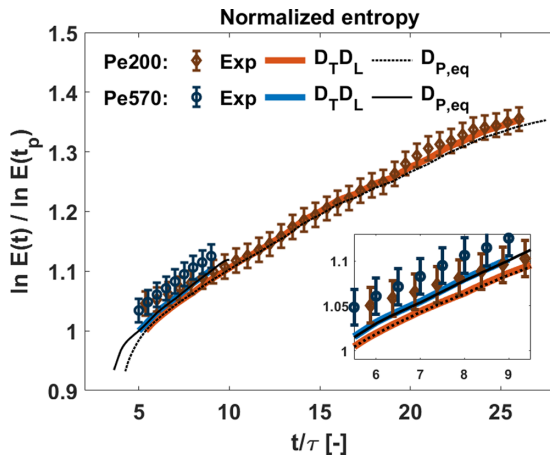


FIG. 4. Normalized entropy at Pe200 and Pe570 in the experiment and the hydrodynamic dispersion model ($D_T D_L$) for the entire time series in which the tracer plume was completely inside the flow-through chamber. Error bars indicate experimental uncertainty. Thin lines correspond to the equivalent pore diffusion model ($D_{P,eq}$).

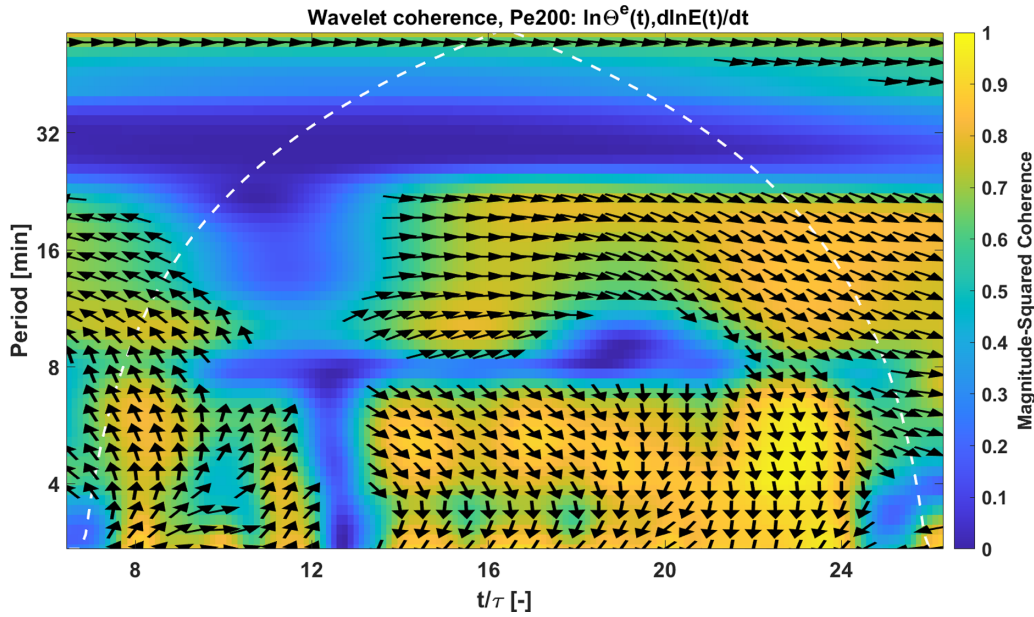


FIG. 5. Squared-wavelet coherence between effective Okubo-Weiss and the rate of increase of the Shannon entropy for Pe200. Dashed lines represent the cone of influence.

normalized mean local dispersion within the plume is changing according to the reservoir fluctuations in the hydrodynamic dispersion model, while in the pore equivalent model, the normalized mean local dispersion within the plume is much smaller. This confirms that the topology of the flow field is the dominant process controlling mixing in this kind of transient flow field. If the Okubo-Weiss field would not control mixing, the entropy rate would not be fluctuating in the equivalent pore diffusion model, or the order of magnitude would be smaller. The results of this study provide experimental evidence of the relation between Okubo-Weiss parameter and plume dilution in porous media.

Finally, the spatial and temporal variations in the local dispersion offer additional insights in the physics of the experiment. For instance, the spatial variability of local dispersion is controlled by the velocity field which, as shown in Fig. 2, has a higher magnitude near the reservoirs. In addition, the spatial averages of the longitudinal and transverse dispersion coefficients within the plume are also changing depending on the distance of the centroid of the plume from each reservoir.

The longitudinal dispersion coefficient in Fig. 7 ranges over several units within the plume surface. However, peak values are concentrated in small areas. This can also explain why processes controlling plume deformation, driven by shearing and stretching and acting over the entire plume, exert a stronger control on mixing than the enhancement in local dispersive processes occurring at very specific locations and for a short time.

V. CONCLUSIONS

In conclusion, the rate of increase of the entropy of a plume depends on the topology of the transient flow field and displays a high coherence with the effective Okubo-Weiss parameter. The model-based interpretation of the performed high-resolution laboratory experiments demonstrates that the effective Okubo-Weiss parameter is the main factor controlling the growth rate of the entropy of a solute plume and thus represents a good proxy for mixing. In the experiments, the variability in the flow field is caused by highly transient

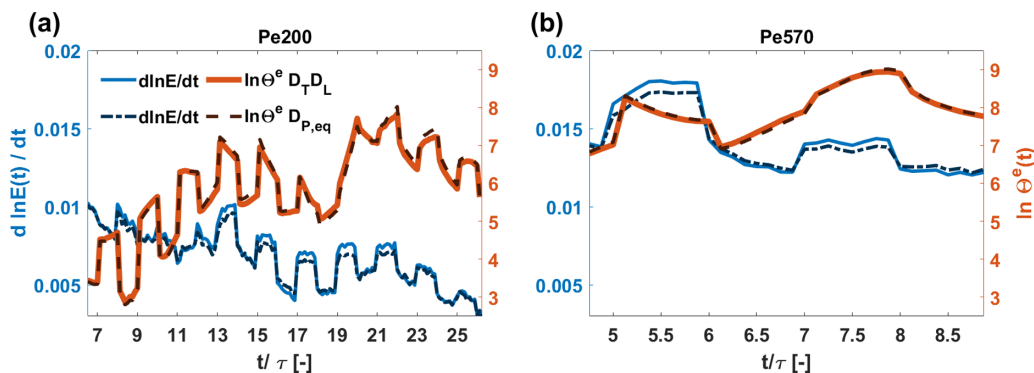


FIG. 6. Rate of increase of the entropy (left axis) and effective Okubo-Weiss (right axis) considering the hydrodynamic dispersion ($D_T D_L$) and the equivalent pore diffusion ($D_{P,eq}$) simulations for Pe200 (a) and Pe570 (b), respectively.

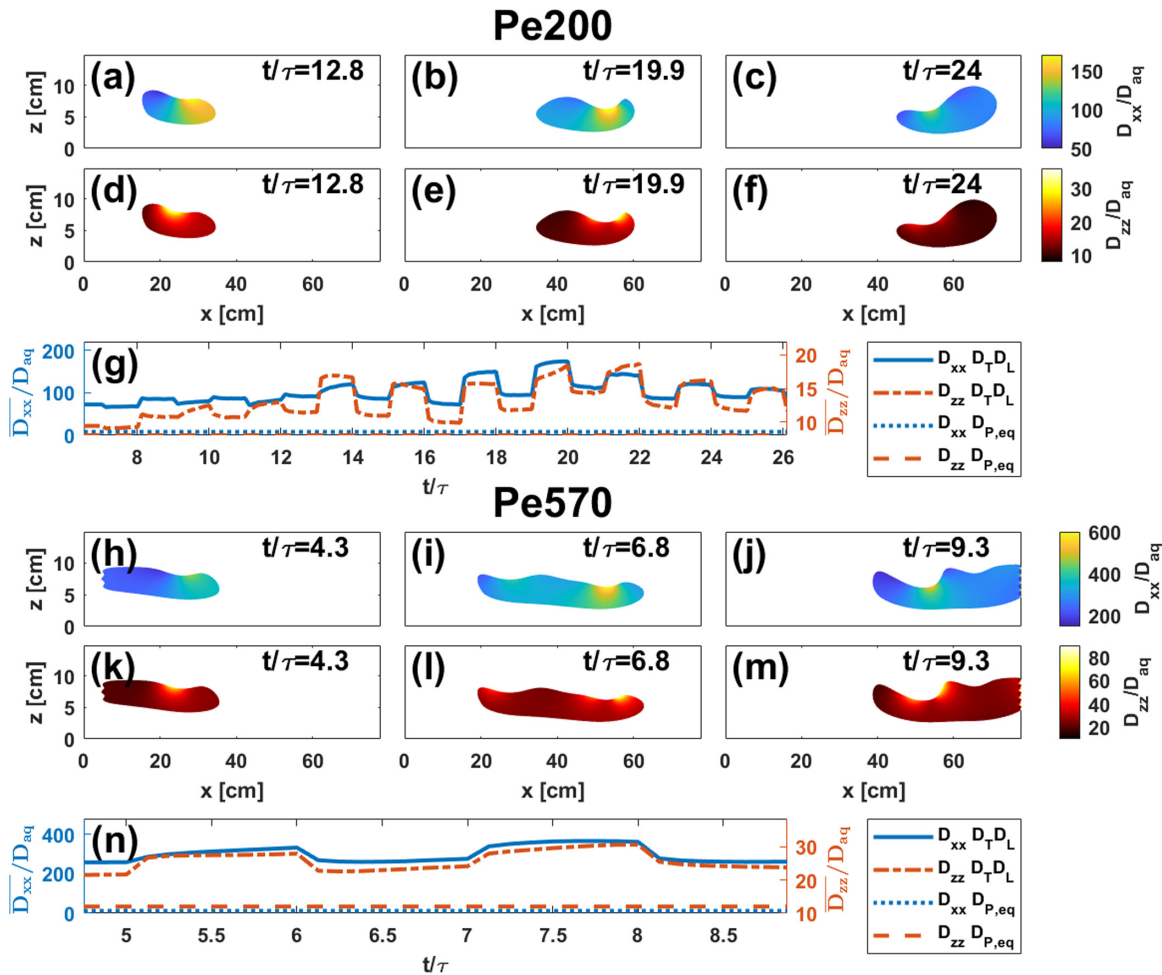


FIG. 7. (a)–(f) Longitudinal and transverse local dispersion (D_{xx} and D_{zz} , respectively) experienced by the plume undergoing hydrodynamic dispersion in the porous medium, $D_T D_L$, at Pe200. (g) Mean of the longitudinal and transverse local dispersion (left and right axis, respectively) considering hydrodynamic dispersion and the equivalent pore diffusion model at Pe200. (h)–(m) and (n) are the same as (a)–(f) and (g) but for Pe570. Results are normalized by the aqueous diffusion coefficient.

boundary conditions, showing that not only heterogeneous permeability fields may display complex mixing dynamics in porous media. Acknowledging the importance of the flow topology to quantify mixing and to understand mixing processes in porous media is relevant for both natural and engineered systems. In particular, our findings can be applied in mixing dynamics for the design of packed bed reactors, and for studying geophysical flows and groundwater aquifers connected to fluctuating surface water bodies (e.g., tidal sea level fluctuations and regulated rivers). Moreover, considering that mixing-controlled reactions are commonly encountered in porous media, we envision future research investigating reactive solute transport based on the analysis of the flow field topology. This will facilitate the understanding of the fate and transport of chemicals, nutrients, and energy fluxes in subsurface formations and at the interface between different environmental compartments.

ACKNOWLEDGMENTS

This research is a result of the UNMIX project (Uncertainties due to boundary conditions in predicting MIXing in groundwater), which is supported by the Deutsche Forschungsgemeinschaft (DFG) through the TUM International Graduate School for Science and Engineering (IGSSE), GSC 81. Financial support for initiating the TUM-DTU collaboration was provided by the Bayerische Forschungsallianz (BayFOR) GmbH, through the Bayerischen Hochschulförderprogramms zur Anbahnung internationaler Forschungskooperationen (Grant No. BayIntAn_TUM_2019_65). M.B.H. also acknowledges the Mexican National Council for Science and Technology (CONACYT) and the Consejo Veracruzano de Investigación Científica y Desarrollo Tecnológico (COVICYDET). Additional financial support for G.C. was provided by the Deutsche Forschungsgemeinschaft (DFG) Project Hydromix (CH981/4-1).

- [1] J.-Y. Chemin, *Astérisque* **230**, 192 (1995).
 [2] G. Chiogna, M. Rolle, A. Bellin, and O. A. Cirpka, *Adv. Water Res.* **73**, 134 (2014).

- [3] S. H. Lee and P. K. Kang, *Phys. Rev. Lett.* **124**, 144501 (2020).
 [4] J. M. Ottino, *Annu. Rev. Fluid Mech.* **22**, 207 (1990).

- [5] R. Turuban, D. R. Lester, T. Le Borgne, and Y. Méheust, *Phys. Rev. Lett.* **120**, 024501 (2018).
- [6] M. Danish, S. Suman, and S. S. Girimaji, *J. Fluid Mech.* **793**, 633 (2016).
- [7] T. Le Borgne, M. Dentz, and E. Villermaux, *Phys. Rev. Lett.* **110**, 204501 (2013).
- [8] F. Brau, G. Schuszter, and A. De Wit, *Phys. Rev. Lett.* **118**, 134101 (2017).
- [9] A. Comolli, A. De Wit, and F. Brau, *Phys. Rev. E* **100**, 052213 (2019).
- [10] R. M. Neupauer, L. J. Sather, D. C. Mays, J. P. Crimaldi, and E. J. Roth, *Water Resour. Res.* **56**, e2019WR026276 (2020).
- [11] M. A. Budroni, V. Upadhyay, and L. Rongy, *Phys. Rev. Lett.* **122**, 244502 (2019).
- [12] J. J. Hidalgo, J. Fe, L. Cueto-Felgueroso, and R. Juanes, *Phys. Rev. Lett.* **109**, 264503 (2012).
- [13] S. Sen, P. Singh, J. Heyman, T. Le Borgne, and A. Bandopadhyay, *Phys. Fluids* **32**, 106602 (2020).
- [14] H. Aref, J. R. Blake, M. Budišić, S. S. S. Cardoso, J. H. E. Cartwright, H. J. H. Clercx, K. El Omari, U. Fuedel, R. Golestanian, E. Guillard *et al.*, *Rev. Mod. Phys.* **89**, 025007 (2017).
- [15] A. C. Bagtzoglou and P. M. Oates, *J. Mater. Civ. Eng.* **19**, 75 (2007).
- [16] P. Sundararajan and A. D. Stroock, *Annu. Rev. Chem. Biomol. Eng.* **3**, 473 (2012).
- [17] A. D. Stroock, S. K. W. Dertinger, A. Ajdari, I. Mezic, H. A. Stone, and G. M. Whitesides, *Science* **295**, 647 (2002).
- [18] E. Villermaux, A. D. Stroock, and H. A. Stone, *Phys. Rev. E* **77**, 015301(R) (2008).
- [19] P. Zhang, S. L. Devries, A. Dathe, and A. C. Bagtzoglou, *Environ. Sci. Technol.* **43**, 6283 (2009).
- [20] P. Rodríguez-Escales, D. Fernández-García, J. Drechsel, A. Folch, and X. Sanchez-Vila, *Water Resour. Res.* **53**, 4376 (2017).
- [21] R. Clemente, F. Sastre, A. Barrero-Gil, and A. Velazquez, *Exp. Thermal Fluid Sci.* **109**, 109846 (2019).
- [22] P. de Anna, T. Le Borgne, M. Dentz, A. M. Tartakovsky, D. Bolster, and P. Davy, *Phys. Rev. Lett.* **110**, 184502 (2013).
- [23] J. Jiménez-Martínez, M. L. Porter, J. D. Hyman, J. W. Carey, and H. S. Viswanathan, *Geophys. Res. Lett.* **43**, 196 (2016).
- [24] M. Souzy, H. Lhuissier, Y. Méheust, T. Le Borgne, and B. Metzger, *J. Fluid Mech.* **891** A16 (2020).
- [25] D. R. Lester, M. Dentz, T. Le Borgne, and F. P. J. de Barros, *J. Fluid Mech.* **855**, 770 (2018).
- [26] R. Turuban, D. R. Lester, J. Heyman, T. Le Borgne, and Y. Méheust, *J. Fluid Mech.* **871**, 562 (2019).
- [27] J. Heyman, D. R. Lester, R. Turuban, Y. Méheust, and T. Le Borgne, *Proc. Natl. Acad. Sci. USA* **117**, 13359 (2020).
- [28] M. Dentz, T. Le Borgne, A. Englert, and B. Bijeljic, *J. Contam. Hydrol.* **120–121**, 1 (2011).
- [29] A. Hernandez-Aguirre, E. Hernandez-Martinez, F. López-Isunza, and C. O. Castillo, *Chem. Eng. J.* **429**, 132061 (2022).
- [30] G. Chiogna, O. A. Cirpka, M. Rolle, and A. Bellin, *Water Resour. Res.* **51**, 261 (2015).
- [31] C. J. Werth, O. A. Cirpka, and P. Grathwohl, *Water Resour. Res.* **42**, W12414 (2006).
- [32] Y. Ye, G. Chiogna, C. Lu, and M. Rolle, *Phys. Rev. E* **102**, 013110 (2020).
- [33] X. Shang, X. Huang, and C. Yang, *Exp. Therm Fluid Sci.* **67**, 57 (2015).
- [34] J. den Toonder, F. Bos, D. Broer, L. Filippini, M. Gillies, J. de Goede, T. Mol, M. Reijmeert, W. Talen, H. Wilderbeek *et al.*, *Lab Chip* **8**, 533 (2008).
- [35] J. Ortega-Casanova and C.-H. Lai, *Comput. Fluids* **168**, 318 (2018).
- [36] M. Di Dato, F. P. J. de Barros, A. Fiori, and A. Bellin, *Water Resour. Res.* **54**, 2095 (2018).
- [37] R. M. Neupauer, J. D. Meiss, and D. C. Mays, *Water Resour. Res.* **50**, 1433 (2014).
- [38] A. N. Piscopo, R. M. Neupauer, and D. C. Mays, *Water Resour. Res.* **49**, 3618 (2013).
- [39] C. J. M. Cremer, I. Neuweiler, M. Bechtold, and J. Vanderborcht, *Vadose Zone J.* **15**, 1 (2016).
- [40] C. J. M. Cremer and I. Neuweiler, *Water Resour. Res.* **55**, 10765 (2019).
- [41] D. C. Mays and R. M. Neupauer, *Water Resour. Res.* **48**, W07501 (2012).
- [42] M. G. Trefry, D. R. Lester, G. Metcalfe, and J. Wu, *Water Resour. Res.* **55**, 3347 (2019).
- [43] C. B. Rizzo, X. Song, F. P. J. de Barros, and X. Chen, *J. Contam. Hydrol.* **235**, 103713 (2020).
- [44] D. J. Goode and L. F. Konikow, *Water Resour. Res.* **26**, 2339 (1990).
- [45] F. R. Phelan, N. R. Hughes, and J. A. Pathak, *Phys. Fluids* **20**, 023101 (2008).
- [46] K. R. Rehfeldt and L. W. Gelhar, *Water Resour. Res.* **28**, 2085 (1992).
- [47] M. Dentz, D. R. Lester, T. Le Borgne, and F. P. J. de Barros, *Phys. Rev. E* **94**, 061102(R) (2016).
- [48] Y. Ye, G. Chiogna, O. A. Cirpka, P. Grathwohl, and M. Rolle, *Phys. Rev. Lett.* **115**, 194502 (2015).
- [49] J.-R. de Dreuzy, J. Carrera, M. Dentz, and T. Le Borgne, *Water Resour. Res.* **48**, W01532 (2012).
- [50] W. Kinzelbach and Ackerer Philippe, *Hydrogéologie* **2**, 197 (1986).
- [51] M. Rolle and T. Le Borgne, *Rev. Mineral. Geochem.* **85**, 111 (2019).
- [52] Y. Ye, G. Chiogna, O. A. Cirpka, P. Grathwohl, and M. Rolle, *Water Resour. Res.* **51**, 5582 (2015).
- [53] R. Sprocati, A. Gallo, R. Sethi, and M. Rolle, *Environ. Sci. Technol.* **55**, 719 (2021).
- [54] P. K. Kitanidis, *Water Resour. Res.* **30**, 2011 (1994).
- [55] A. Okubo, *Deep Sea Res. Oceanogr. Abstr.* **17**, 445 (1970).
- [56] J. Weiss, *Physica D (Amsterdam, Neth.)* **48**, 273 (1991).
- [57] P. Perlekar, S. S. Ray, D. Mitra, and R. Pandit, *Phys. Rev. Lett.* **106**, 054501 (2011).
- [58] B. Kadoch, D. Del-Castillo-Negrete, W. J. T. Bos, and K. Schneider, *Phys. Rev. E* **83**, 036314 (2011).
- [59] N. C. Hurst, J. R. Danielson, D. H. E. Dubin, and C. M. Surko, *Phys. Rev. Lett.* **117**, 235001 (2016).
- [60] E. Casella, A. Molcard, and A. Provenzale, *J. Mar. Syst.* **88**, 12 (2011).
- [61] X. Geng, H. A. Michael, M. C. Boufadel, F. J. Molz, F. Gerges, and K. Lee, *Geophys. Res. Lett.* **47**, e2020GL089612 (2020).
- [62] G. Rouillet and P. Klein, *Phys. Rev. Lett.* **104**, 218501 (2010).
- [63] C. Blanch-Mercader, V. Yashunsky, S. Garcia, G. Duclos, L. Giomi, and P. Silberzan, *Phys. Rev. Lett.* **120**, 208101 (2018).

- [64] F. Li, J. Liu, J. Ren, X. Cao, and Y. Zhu, *Int. J. Heat Mass Transfer* **96**, 287 (2016).
- [65] F. P. J. de Barros, M. Dentz, J. Koch, and W. Nowak, *Geophys. Res. Lett.* **39**, L08404 (2012).
- [66] E. E. Wright, D. H. Richter, and D. Bolster, *Phys. Rev. Fluids* **2**, 114501 (2017).
- [67] N. B. Engdahl, D. A. Benson, and D. Bolster, *Phys. Rev. E* **90**, 051001(R) (2014).
- [68] Y. Ye, G. Chiogna, O. A. Cirpka, P. Grathwohl, and M. Rolle, *Phys. Rev. E* **94**, 013113 (2016).
- [69] M. Rolle, C. Eberhardt, G. Chiogna, O. A. Cirpka, and P. Grathwohl, *J. Contam. Hydrol.* **110**, 130 (2009).
- [70] G. Sposito, *Water Resour. Res.* **42**, W06D03 (2006).
- [71] F. Ziliotto, M. Basilio Hazas, M. Rolle, and G. Chiogna, *Geophys. Res. Lett.* **48**, e2021GL095336 (2021).
- [72] M. S. Cho, F. Solano, N. R. Thomson, M. G. Trefry, D. R. Lester, and G. Metcalfe, *Groundwater Monit. Rem.* **39**, 23 (2019).
- [73] M. Dentz and J. Carrera, *Phys. Rev. E* **68**, 036310 (2003).
- [74] M. Dentz and J. Carrera, *Water Resour. Res.* **41**, W08414 (2005).
- [75] D. Bolster, M. Dentz, and J. Carrera, *Water Resour. Res.* **45**, W05408 (2009).
- [76] C. M. Haberer, M. Rolle, O. A. Cirpka, and P. Grathwohl, *Vadose Zone J.* **11**, vzj2011.0056 (2012).
- [77] S. Jaeger, M. Ehni, C. Eberhardt, M. Rolle, P. Grathwohl, and G. Gauglitz, *Anal. Bioanal. Chem.* **395**, 1867 (2009).
- [78] S. E. Boyce, R. T. Hanson, I. Ferguson, W. Schmid, W. Henson, T. Reimann, S. M. Mehl, and M. M. Earll, *U.S. Geological Survey, Techniques and Methods 6-A60*, 435 (2020).
- [79] M. J. Tonkin, V. Bedekar, E. D. Morway, and C. D. Langevin, *MT3D-USGS: Groundwater Solute Transport Simulator for MODFLOW* (U.S. Geological Survey, Reston VA, 2016).
- [80] J. R. F. Guedes de Carvalho and J. M. P. Q. Delgado, *Chem. Eng. Sci.* **60**, 365 (2005).
- [81] M. Muniruzzaman and M. Rolle, *Water Resour. Res.* **53**, 1189 (2017).
- [82] G. Chiogna, C. Eberhardt, P. Grathwohl, O. A. Cirpka, and M. Rolle, *Environ. Sci. Technol.* **44**, 688 (2010).
- [83] Y. Ye, G. Chiogna, O. Cirpka, P. Grathwohl, and M. Rolle, *J. Contam. Hydrol.* **172**, 33 (2015).
- [84] A. Grinsted, J. C. Moore, and S. Jevrejeva, *Nonlinear Processes Geophys.* **11**, 561 (2004).